DOF Augmentation via IRS for Line-of-Sight Communication

Heedong Do
POSTECH, Korea
Graduate Student Member, IEEE
Email: doheedong@postech.ac.kr

Namyoon Lee
Korea University, Korea
Senior Member, IEEE
Email: namyoon@korea.ac.kr

Angel Lozano
Univ. Pompeu Fabra (UPF), Spain
Fellow, IEEE
Email: angel.lozano@upf.edu

***Abstract*—This paper analyzes the effect of deploying an intelligent reflective surface (IRS) in line-of-sight conditions at sub-terahertz frequencies. Besides the more obvious benefits of enhancing the received power and sidestepping blockages, at these frequencies an IRS can augment the number of spatial degrees of freedom even as the transmitter and receiver footprints remain fixed. This possibility, which is revealed only if the curved nature of the wavefronts is accounted for, results from the IRS acting as a lens that enables resolving denser spatial multiplexings. Provided the signal-to-noise ratio is minimally high, this DOF augmentation then translates to a hefty improvement in spectral efficiency.**

I. Introduction

The appetite for ever higher frequencies on which to communicate wirelessly is insatiable, with the next frontier being the sub-terahertz band (0.1–1 THz) [1]–[3]. At these frequencies, the propagation is ray-like [4], [5] and the availability of a line-of-sight (LOS) component or some strong reflection largely determines the performance. Hence, these frequencies are mostly envisioned for short-range transmissions, which go hand in hand with denser networks. Such densification need not entail additional full-stack access points, and relays could be deployed in their stead. Or, as an emerging alternative, the densification could be aided by intelligent reflecting surfaces (IRSs), which are passive, devoid of radio-frequency chains and baseband processing [6]–[8]. Accordingly, the main motivating application for IRSs at sub-terahertz frequencies is to bypass obstructions, yet, as expounded in this paper, a potentially more impactful benefit may arise from their deployment: an enrichment in the number of spatial degrees of freedom (DOF). While an inherently asymptotic notion, which describes the scaling of the spectral efficiency with the received power [9, Sec. 4.2], the number of DOF translates directly to the number of concurrent signal streams that can be communicated and is therefore a quantity of prime interest.

LOS communication at sub-terahertz frequencies may enjoy a multiplicity of DOF, as transmitter and receiver feature arrays large enough relative to the wavelength and to the transmission range that individual antennas can be resolved at the other end of the link even without multipath components [10]–[21]. Indeed, the DOF over an LOS link scales with the product of the transmit and receive footprints measured in wavelengths [22], reflecting the fact that a larger receiver enables a denser spatial multiplexing at the transmitter, and vice versa.

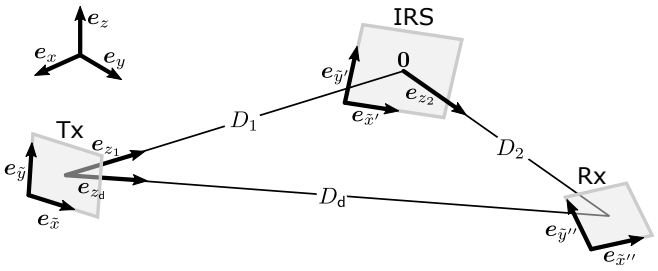

Fig. 1. Coordinate systems.

Now consider two LOS links cascaded via an IRS. Since it serves as receiver for the first link, and as transmitter for the second, the IRS can simultaneously augment the DOF over each link, and thus for the overall channel. The remarkable conclusion is that a large-aperture IRS, when properly configured, can potentially unlock DOF without the transmitter or receiver increasing their footprints, thereby circumventing physical limitations at access points (APs) and devices. This newfound possibility could not be anticipated under classical planar wavefront models. Rather, it comes to the fore once the curved nature of the wavefronts is taken into consideration, implying that an inadequate channel model may greatly underestimate the potential of sub-terahertz communication.

This paper confirms the reality of this DOF augmentation, exemplifying its impact on the achievable spectral efficiencies with uniform planar arrays (UPAs).

II. LOS Channel Model

Consider an N_{t}-antenna transmitter, an N_{r}-antenna receiver, and an M-element IRS. The transmitter, IRS, and receiver are in the vicinity of $-D_1\boldsymbol{e}_{z_1}$, $(0,0,0)$, and $D_2\boldsymbol{e}_{z_2}$, with (x_m, y_m, z_m), $(x'_\ell, y'_\ell, z'_\ell)$, and (x''_n, y''_n, z''_n) the locations of the mth transmit antenna, ℓth IRS element, and nth receive antenna, respectively (see Fig. 1). Denoting the distance from the mth transmit to the nth receive antenna by

$$D^{\mathsf{direct}}_{n,m} = \|(x''_n, y''_n, z''_n) - (x_m, y_m, z_m)\|, \tag{1}$$

the complex baseband channel coefficient is

$$h^{\mathsf{direct}}_{n,m} = \frac{\sqrt{G_{\mathrm{t}}G_{\mathrm{r}}}\lambda}{4\pi D^{\mathsf{direct}}_{n,m}} e^{-j\frac{2\pi}{\lambda}D^{\mathsf{direct}}_{n,m}} \tag{2}$$

where λ is the wavelength while G_{t} and G_{r} are the transmit and receive antenna gains, respectively. Similarly, given

$$D_{\ell,m}^{\mathsf{Tx\text{-}IRS}} = \|(x'_\ell, y'_\ell, z'_\ell) - (x_m, y_m, z_m)\| \tag{3}$$

$$D_{n,\ell}^{\mathsf{IRS\text{-}Rx}} = \|(x''_n, y''_n, z''_n) - (x'_\ell, y'_\ell, z'_\ell)\|, \tag{4}$$

the channel coefficients for the transmitter-IRS and the IRS-receiver channels are

$$h_{\ell,m}^{\mathsf{Tx\text{-}IRS}} = \frac{\sqrt{G_{\mathrm{t}} G_{\mathrm{i}}}\lambda}{4\pi D_{\ell,m}^{\mathsf{Tx\text{-}IRS}}} e^{-j\frac{2\pi}{\lambda} D_{\ell,m}^{\mathsf{Tx\text{-}IRS}}} \tag{5}$$

$$h_{n,\ell}^{\mathsf{IRS\text{-}Rx}} = \frac{\sqrt{G_{\mathrm{i}} G_{\mathrm{r}}}\lambda}{4\pi D_{n,\ell}^{\mathsf{IRS\text{-}Rx}}} e^{-j\frac{2\pi}{\lambda} D_{n,\ell}^{\mathsf{IRS\text{-}Rx}}} \tag{6}$$

with G_{i} the IRS element gain.

Under the proviso that the arrays and the IRS are small relative to the transmission range, the magnitudes of $h_{n,m}^{\mathsf{direct}}$, $h_{\ell,m}^{\mathsf{Tx\text{-}IRS}}$, and $h_{n,\ell}^{\mathsf{IRS\text{-}Rx}}$ are essentially constant over the indices. Factoring out these magnitudes, the respective channel matrices satisfy

$$[\boldsymbol{H}_{\mathsf{d}}]_{n,m} = e^{-j\frac{2\pi}{\lambda} D_{n,m}^{\mathsf{direct}}} \tag{7}$$

$$[\boldsymbol{H}_1]_{\ell,m} = e^{-j\frac{2\pi}{\lambda} D_{\ell,m}^{\mathsf{Tx\text{-}IRS}}} \tag{8}$$

$$[\boldsymbol{H}_2]_{n,\ell} = e^{-j\frac{2\pi}{\lambda} D_{n,\ell}^{\mathsf{IRS\text{-}Rx}}}. \tag{9}$$

Letting $D_{\mathsf{d}} = \|D_1 \boldsymbol{e}_{z_1} + D_2 \boldsymbol{e}_{z_2}\|$, the unit vectors $\boldsymbol{e}_{z_1}$, $\boldsymbol{e}_{z_2}$ and

$$\boldsymbol{e}_{z_{\mathsf{d}}} = \frac{D_1 \boldsymbol{e}_{z_1} + D_2 \boldsymbol{e}_{z_2}}{D_{\mathsf{d}}} \tag{10}$$

enable three local coordinate systems: one for the transmitter-IRS link, another for the IRS-receiver link, and the other for the transmitter-receiver link (see Fig. 1).

With planar arrays, there are sure to be orthonormal sets $\{\boldsymbol{e}_{\tilde{x}}, \boldsymbol{e}_{\tilde{y}}\}$, $\{\boldsymbol{e}'_{\tilde{x}}, \boldsymbol{e}'_{\tilde{y}}\}$, $\{\boldsymbol{e}''_{\tilde{x}}, \boldsymbol{e}''_{\tilde{y}}\}$ and two-dimensional coordinates

$$\left[\tilde{x}_m \ \tilde{y}_m\right]^\top, \left[\tilde{x}'_\ell \ \tilde{y}'_\ell\right]^\top, \left[\tilde{x}''_n \ \tilde{y}''_n\right]^\top$$

satisfying

$$\begin{bmatrix} x_m \\ y_m \\ z_m \end{bmatrix} = -D_1 \boldsymbol{e}_{z_1} + \begin{bmatrix} \boldsymbol{e}_{\tilde{x}} & \boldsymbol{e}_{\tilde{y}} \end{bmatrix} \begin{bmatrix} \tilde{x}_m \\ \tilde{y}_m \end{bmatrix} \tag{11}$$

$$\begin{bmatrix} x'_\ell \\ y'_\ell \\ z'_\ell \end{bmatrix} = \begin{bmatrix} \boldsymbol{e}_{\tilde{x}'} & \boldsymbol{e}_{\tilde{y}'} \end{bmatrix} \begin{bmatrix} \tilde{x}'_\ell \\ \tilde{y}'_\ell \end{bmatrix} \tag{12}$$

$$\begin{bmatrix} x''_n \\ y''_n \\ z''_n \end{bmatrix} = D_2 \boldsymbol{e}_{z_2} + \begin{bmatrix} \boldsymbol{e}_{\tilde{x}''} & \boldsymbol{e}_{\tilde{y}''} \end{bmatrix} \begin{bmatrix} \tilde{x}''_n \\ \tilde{y}''_n \end{bmatrix}. \tag{13}$$

To make things precise for UPAs, consider the transmitter specifically. Conveniently selecting the axes $\boldsymbol{e}_{\tilde{x}}$ and $\boldsymbol{e}_{\tilde{y}}$, the $N_{\mathrm{t},x} \times N_{\mathrm{t},y}$ transmit UPA, with footprint $L_{\mathrm{t},x} \times L_{\mathrm{t},y}$, has the antennas at coordinates

$$\left\{ \begin{bmatrix} \tilde{x}_m \\ \tilde{y}_m \end{bmatrix} | \, m = 1, \ldots, N_{\mathrm{t}} \right\} = \tag{14}$$

$$\left(d_{\mathrm{t},x}\left(\mathbb{Z} - \tfrac{1}{2}\right) \times d_{\mathrm{t},y}\left(\mathbb{Z} - \tfrac{1}{2}\right)\right) \cap \left(L_{\mathrm{t},x}\left[-\tfrac{1}{2}, \tfrac{1}{2}\right] \times L_{\mathrm{t},y}\left[-\tfrac{1}{2}, \tfrac{1}{2}\right]\right)$$

where $d_{\mathrm{t},x} = \frac{L_{\mathrm{t},x}}{N_{\mathrm{t},x}}$ and $d_{\mathrm{t},y} = \frac{L_{\mathrm{t},y}}{N_{\mathrm{t},y}}$ while $\times$ denotes the Cartesian product of sets. The receiver and the IRS are similarly described, with subscripts "r" and "i" in lieu of "t." Also, (14) can be tweaked if either number of antennas is odd rather than even.

III. Direct Transmission

The relationship between the transmit signal $\boldsymbol{s}$ and the receive signal $\boldsymbol{y}$ is

$$\boldsymbol{y} = \boldsymbol{H}_{\mathsf{d}} \boldsymbol{s} + \boldsymbol{v} \tag{15}$$

given $\boldsymbol{H}_{\mathsf{d}} \in \mathbb{C}^{N_{\mathrm{r}} \times N_{\mathrm{t}}}$ and with $\boldsymbol{v} \sim \mathcal{N}_{\mathbb{C}}(\boldsymbol{0}, \boldsymbol{I})$ the noise. The magnitude that was factored out of $\boldsymbol{H}_{\mathsf{d}}$ is incorporated into

$$\mathsf{SNR}_{\mathsf{d}} = \mathsf{L}_{\mathsf{d}} \frac{P_{\mathrm{t}}}{BN_0}, \tag{16}$$

where $\mathsf{L}_{\mathsf{d}} = \frac{\lambda^2 G_{\mathrm{t}} G_{\mathrm{r}}}{(4\pi D_{\mathsf{d}})^2}$ with P_{t} the transmit power, B the bandwidth, and N_0 the noise spectral density. By letting $\boldsymbol{s} \sim \mathcal{N}_{\mathbb{C}}(\boldsymbol{0}, \boldsymbol{Q})$, the transmit power constraint can be written as $\mathrm{tr}(\boldsymbol{Q}) = \mathsf{SNR}_{\mathsf{d}}$ and, with $\sigma_n(\cdot)$ denoting the nth singular value of a matrix, the direct channel capacity is

$$C_{\mathsf{d}} = \max_{\substack{\sum_n p_n = \mathsf{SNR}_{\mathsf{d}} \\ p_n \geq 0}} \sum_n \log_2\Big(1 + p_n \sigma_n^2(\boldsymbol{H}_{\mathsf{d}})\Big). \tag{17}$$

As the arrays grow and densify, the singular values polarize into two levels, namely[1]

$$(\sigma_1(\boldsymbol{H}_{\mathsf{d}}), \sigma_2(\boldsymbol{H}_{\mathsf{d}}), \ldots) \tag{18}$$

$$\approx \lambda D_{\mathsf{d}} \sqrt{\frac{N_{\mathrm{t}} N_{\mathrm{r}}}{\mathsf{area}(T_{\mathsf{d}})\mathsf{area}(R_{\mathsf{d}})}} (\underbrace{1, \ldots, 1}_{\mathsf{DOF}_{\mathsf{d}}}, 0, \ldots)$$

where $\mathsf{DOF}_{\mathsf{d}} = \dfrac{\mathsf{area}(T_{\mathsf{d}})\mathsf{area}(R_{\mathsf{d}})}{(\lambda D_{\mathsf{d}})^2}$ with[2]

$$T_{\mathsf{d}} = \begin{bmatrix} \boldsymbol{e}_{x_{\mathsf{d}}}^\top \\ \boldsymbol{e}_{y_{\mathsf{d}}}^\top \end{bmatrix} \begin{bmatrix} \boldsymbol{e}_{\tilde{x}} & \boldsymbol{e}_{\tilde{y}} \end{bmatrix} \left(L_{\mathrm{t},x}\left[-\tfrac{1}{2}, \tfrac{1}{2}\right] \times L_{\mathrm{t},y}\left[-\tfrac{1}{2}, \tfrac{1}{2}\right]\right) \tag{19}$$

$$R_{\mathsf{d}} = \begin{bmatrix} \boldsymbol{e}_{x_{\mathsf{d}}}^\top \\ \boldsymbol{e}_{y_{\mathsf{d}}}^\top \end{bmatrix} \begin{bmatrix} \boldsymbol{e}_{\tilde{x}'} & \boldsymbol{e}_{\tilde{y}'} \end{bmatrix} \left(L_{\mathrm{r},x}\left[-\tfrac{1}{2}, \tfrac{1}{2}\right] \times L_{\mathrm{r},y}\left[-\tfrac{1}{2}, \tfrac{1}{2}\right]\right). \tag{20}$$

From (19), T_{d} corresponds to the projection of the transmitter footprint

$$\begin{bmatrix} \boldsymbol{e}_{\tilde{x}} & \boldsymbol{e}_{\tilde{y}} \end{bmatrix} \left(L_{\mathrm{t},x}\left[-\tfrac{1}{2}, \tfrac{1}{2}\right] \times L_{\mathrm{t},y}\left[-\tfrac{1}{2}, \tfrac{1}{2}\right]\right) \tag{21}$$

onto the space spanned by $\boldsymbol{e}_{x_{\mathsf{d}}}$ and $\boldsymbol{e}_{y_{\mathsf{d}}}$. Since

$$\left|\det\left(\begin{bmatrix} \boldsymbol{e}_{x_{\mathsf{d}}}^\top \\ \boldsymbol{e}_{y_{\mathsf{d}}}^\top \end{bmatrix} \begin{bmatrix} \boldsymbol{e}_{\tilde{x}} & \boldsymbol{e}_{\tilde{y}} \end{bmatrix}\right)\right| \tag{22}$$

equals the cosine of the dihedral angle between two planes, this determinant reduces to $|\boldsymbol{e}_{z_{\mathsf{d}}}^\top \boldsymbol{e}_{\tilde{z}}|$, where $\boldsymbol{e}_{z_{\mathsf{d}}} = \boldsymbol{e}_{x_{\mathsf{d}}} \times \boldsymbol{e}_{y_{\mathsf{d}}}$ and $\boldsymbol{e}_{\tilde{z}} = \boldsymbol{e}_{\tilde{x}} \times \boldsymbol{e}_{\tilde{y}}$ are the unit vectors completing the local coordinate systems; here, $\times$ denotes the cross-product of vectors. Ditto for R_{d}, such that

$$\mathsf{area}(T_{\mathsf{d}}) = L_{\mathrm{t},x} L_{\mathrm{t},y} \, |\boldsymbol{e}_{z_{\mathsf{d}}}^\top \boldsymbol{e}_{\tilde{z}}| \tag{23}$$

$$\mathsf{area}(R_{\mathsf{d}}) = L_{\mathrm{r},x} L_{\mathrm{r},y} \, |\boldsymbol{e}_{z_{\mathsf{d}}}^\top \boldsymbol{e}_{\tilde{z}'}|. \tag{24}$$

[1]For details on how (18) and (30) sharpen as the footprints and numbers of antennas increase, see [23, Secs. IV-V].

[2]Hereafter, for a matrix $\boldsymbol{A}$ and a set $\mathcal{B}$ of vectors, $\boldsymbol{A}\mathcal{B} = \{\boldsymbol{A}\boldsymbol{b} | \boldsymbol{b} \in \mathcal{B}\}$.

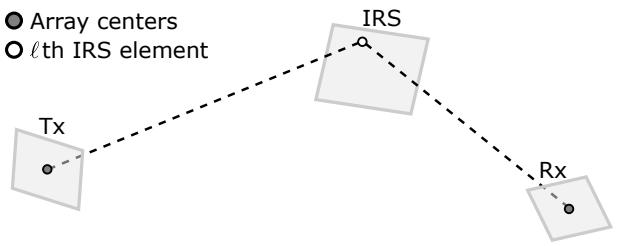

Fig. 2. Intuitive geometric interpretation of the proposed phase shifts in (28)

IV. IRS-Assisted Transmission

With the IRS in place, the relation between the transmit signal $\boldsymbol{s}$ and the receive signal $\boldsymbol{y}$ becomes

$$\boldsymbol{y} = \boldsymbol{H}_2 \boldsymbol{\Phi} \boldsymbol{H}_1 \boldsymbol{s} + \boldsymbol{v} \tag{25}$$

given $\boldsymbol{H}_2 \in \mathbb{C}^{N_\mathrm{r} \times M}$ as the IRS-receiver channel matrix, $\boldsymbol{\Phi} = \mathrm{diag}(e^{j\phi_1}, \ldots, e^{j\phi_M}) \in \mathbb{C}^{M \times M}$ as the phase shift matrix at the IRS, and $\boldsymbol{H}_1 \in \mathbb{C}^{M \times N_\mathrm{t}}$ as the transmitter-IRS channel. The composite channel is $\boldsymbol{H}_\mathsf{a} = \boldsymbol{H}_2 \boldsymbol{\Phi} \boldsymbol{H}_1$. The distance-related factors that were normalized out of $\boldsymbol{H}_1$ and $\boldsymbol{H}_2$ are incorporated into

$$\mathsf{SNR}_\mathsf{a} = \mathsf{L}_1 \mathsf{L}_2 \frac{P_\mathrm{t}}{BN_0} \tag{26}$$

where $\mathsf{L}_1 = \frac{\lambda^2 G_\mathrm{t} G_\mathrm{i}}{(4\pi D_1)^2}$ and $\mathsf{L}_2 = \frac{\lambda^2 G_\mathrm{i} G_\mathrm{r}}{(4\pi D_2)^2}$. The highest spectral efficiency with a certain $\boldsymbol{\Phi}$ is

$$\max_{\substack{\sum_n p_n = \mathsf{SNR}_\mathsf{a} \\ p_n \geq 0}} \sum_n \log_2\Big(1 + p_n \sigma_n^2(\boldsymbol{H}_\mathsf{a})\Big). \tag{27}$$

With the arrays being small relative to the range, such that the spherical wavefronts are parabolic over those arrays, it is shown in [23] that the phase shifts that asymptotically (in the IRS footprint) maximize (27) are those that have the IRS act as a lens, inverting the curvature of the wavefronts impinging on it. That corresponds to

$$\phi_\ell = \frac{2\pi}{\lambda}\left(\left\|\begin{bmatrix} x'_\ell \\ y'_\ell \\ z'_\ell \end{bmatrix} + D_1 \boldsymbol{e}_{z_1}\right\| + \left\|\begin{bmatrix} x'_\ell \\ y'_\ell \\ z'_\ell \end{bmatrix} - D_2 \boldsymbol{e}_{z_2}\right\|\right), \tag{28}$$

which is tantamount to (see Fig. 2)

$$\phi_\ell = 2\pi \frac{\text{length of dotted line}}{\lambda} \tag{29}$$

where the dotted line connects the center of the transmit array with the ℓth IRS element, and then on to the center of the receive array.

As the arrays and the IRS grow and densify, the singular values again polarize into two levels, in this case[1]

$$\begin{aligned}&(\sigma_1(\boldsymbol{H}_\mathsf{a}), \sigma_2(\boldsymbol{H}_\mathsf{a}), \ldots) \\ &\approx \lambda^2 D_1 D_2 \frac{M}{\mathsf{area}(I_\mathsf{a})} \sqrt{\frac{N_\mathrm{t} N_\mathrm{r}}{\mathsf{area}(T_\mathsf{a})\mathsf{area}(R_\mathsf{a})}} (\underbrace{1, \ldots, 1}_{\mathsf{DOFa}}, 0, \ldots)\end{aligned} \tag{30}$$

where[3] $\mathsf{DOF}_\mathsf{a} = \dfrac{\mathsf{area}(I_\mathsf{a})\mathsf{area}\big(T_\mathsf{a} \cap (-R_\mathsf{a})\big)}{\lambda^2 D_1 D_2}$ with

$$\begin{aligned} T_\mathsf{a} = \sqrt{\frac{D_2}{D_1}} \begin{bmatrix} \boldsymbol{e}_{\tilde{x}'}^\top \\ \boldsymbol{e}_{\tilde{y}'}^\top \end{bmatrix} \left(\boldsymbol{I} - \boldsymbol{e}_{z_1} \boldsymbol{e}_{z_1}^\top\right) \begin{bmatrix} \boldsymbol{e}_{\tilde{x}} & \boldsymbol{e}_{\tilde{y}} \end{bmatrix} \\ \cdot \Big(L_{\mathrm{t},x}\big[-\tfrac{1}{2}, \tfrac{1}{2}\big] \times L_{\mathrm{t},y}\big[-\tfrac{1}{2}, \tfrac{1}{2}\big]\Big) \end{aligned} \tag{31}$$

$$I_\mathsf{a} = L_{\mathrm{i},x}\big[-\tfrac{1}{2}, \tfrac{1}{2}\big] \times L_{\mathrm{i},y}\big[-\tfrac{1}{2}, \tfrac{1}{2}\big] \tag{32}$$

$$\begin{aligned} R_\mathsf{a} = \sqrt{\frac{D_1}{D_2}} \begin{bmatrix} \boldsymbol{e}_{\tilde{x}'}^\top \\ \boldsymbol{e}_{\tilde{y}'}^\top \end{bmatrix} \left(\boldsymbol{I} - \boldsymbol{e}_{z_2} \boldsymbol{e}_{z_2}^\top\right) \begin{bmatrix} \boldsymbol{e}_{\tilde{x}''} & \boldsymbol{e}_{\tilde{y}''} \end{bmatrix} \\ \cdot \Big(L_{\mathrm{r},x}\big[-\tfrac{1}{2}, \tfrac{1}{2}\big] \times L_{\mathrm{r},y}\big[-\tfrac{1}{2}, \tfrac{1}{2}\big]\Big). \end{aligned} \tag{33}$$

Rewriting (31) as

$$\begin{aligned} T_\mathsf{a} = \sqrt{\frac{D_2}{D_1}} \underbrace{\begin{bmatrix} \boldsymbol{e}_{\tilde{x}'}^\top \\ \boldsymbol{e}_{\tilde{y}'}^\top \end{bmatrix} \begin{bmatrix} \boldsymbol{e}_{x_1} & \boldsymbol{e}_{y_1} \end{bmatrix}}_{\text{2nd projection}} \underbrace{\begin{bmatrix} \boldsymbol{e}_{x_1}^\top \\ \boldsymbol{e}_{y_1}^\top \end{bmatrix} \begin{bmatrix} \boldsymbol{e}_{\tilde{x}} & \boldsymbol{e}_{\tilde{y}} \end{bmatrix}}_{\text{1st projection}} \\ \cdot \Big(L_{\mathrm{t},x}\big[-\tfrac{1}{2}, \tfrac{1}{2}\big] \times L_{\mathrm{t},y}\big[-\tfrac{1}{2}, \tfrac{1}{2}\big]\Big) \end{aligned} \tag{34}$$

evidences that the transmitter footprint undergoes two projections, first on the span of $\boldsymbol{e}_{x_1}$ and $\boldsymbol{e}_{x_2}$, and subsequently onto $\boldsymbol{e}_{\tilde{x}'}$ and $\boldsymbol{e}_{\tilde{y}'}$. That amounts to projecting the transmitter on the plane orthogonal to the transmitter-IRS axis, and then onto the IRS itself. The counterparts to the direct-transmission results in (23) and (24) are then

$$\mathsf{area}(T_\mathsf{a}) = \frac{D_2}{D_1} L_{\mathrm{t},x} L_{\mathrm{t},y} \, |\boldsymbol{e}_{z_1}^\top \boldsymbol{e}_{\tilde{z}}| |\boldsymbol{e}_{z_1}^\top \boldsymbol{e}_{\tilde{z}'}| \tag{35}$$

$$\mathsf{area}(R_\mathsf{a}) = \frac{D_1}{D_2} L_{\mathrm{r},x} L_{\mathrm{r},y} \, |\boldsymbol{e}_{z_2}^\top \boldsymbol{e}_{\tilde{z}'}| |\boldsymbol{e}_{z_2}^\top \boldsymbol{e}_{\tilde{z}''}|, \tag{36}$$

where newly introduced unit vectors complete their own local coordinate systems.

From the expression for DOF_a, a number of insights can be gleaned:

- Crystallizing the intuition advanced in Sec. I, the DOF in the presence of the IRS scale with its aperture.
- The projected transmit and receive footprints affect the DOF through their intersection. (Sensibly, this indicates that the bottleneck is the smallest of the two projected footprints if one fits within the other.)
- The projected footprints are modified by respective factors that depend on D_1 and D_2, factors that do not cancel out because $\mathsf{area}(T_\mathsf{a} \cap (-R_\mathsf{a})) \neq \mathsf{area}\big(rT_\mathsf{a} \cap \big(-\frac{1}{r} R_\mathsf{a}\big)\big)$. These distance-dependent factors reflect how effective the IRS lensing effect is, depending on the distances: if $D_1/D_2 \gg 1$, then the transmitter appears small and the receiver large from the vantage of the IRS, and vice versa.

The distance-dependent factors provide guidance on the preferred IRS placement, which—from an DOF standpoint, at high SNR—should render $\mathsf{area}(T_\mathsf{a})$ and $\mathsf{area}(R_\mathsf{a})$ comparable. This points to a strategy of deploying the IRS closer to transmitter or receiver, whichever has the smaller footprint, and this

[3]The negative sign applied to R_a, which reflects a signal inversion, entails flipping R_a relative to the origin.

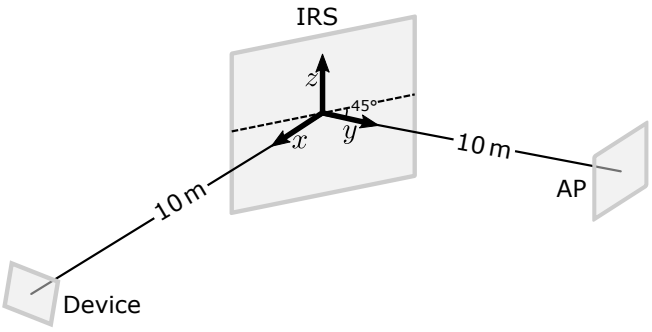

Fig. 3. Geometry for the examples. The AP is parallel to the xz-plane; other orientations would simply entail the appropriate projection.

TABLE I
PARAMETERS

$G_\mathrm{t}=G_\mathrm{r}$ [dBi]	G_i [dBi]	λ [m]	L_d [dB]	L_1 [dB]	L_2 [dB]
10	0	0.001	-85.0	-92.0	-92.0
P_t [dBm]	B [GHz]	N_0 [dBm/GHz]	$\frac{P_\mathrm{t}}{BN_0}$ [dB]	SNR_d [dB]	SNR_a [dB]
10	1	-74.0	84.0	-1.0	-100.0

differs from the deployment strategy when the objective is to maximize the received power [24], [25]. In particular, if the footprints are equal, then the preferred placement would be half-way down the link to maximize the DOF while adjacent to transmitter or receiver to maximize the received power.

We hasten to add that, for $T_\mathsf{a} \subset -R_\mathsf{a}$ or $T_\mathsf{a} \supset -R_\mathsf{a}$, with the apertures being sufficiently large, the proposed phase shift turns out to be optimum not only in terms of DOF, but in terms of spectral efficiency at every SNR [23].

V. Planar Wavefront Model

As the communication range grows and/or the array footprints shrink, relative to the wavelength, the wavefronts go from approximately parabolic to progressively linear, i.e.,

$$[\boldsymbol{H}_\mathsf{d}]_{n,m} \approx \exp\left(-j\frac{2\pi}{\lambda}\left(\boldsymbol{e}_{z_\mathsf{d}}^\top\begin{bmatrix}x_n''\\y_n''\\z_n''\end{bmatrix} - \boldsymbol{e}_{z_\mathsf{d}}^\top\begin{bmatrix}x_m\\y_m\\z_m\end{bmatrix}\right)\right) \tag{37}$$

$$[\boldsymbol{H}_1]_{\ell,m} \approx \exp\left(-j\frac{2\pi}{\lambda}\left(\boldsymbol{e}_{z_1}^\top\begin{bmatrix}x_\ell'\\y_\ell'\\z_\ell'\end{bmatrix} - \boldsymbol{e}_{z_1}^\top\begin{bmatrix}x_m\\y_m\\z_m\end{bmatrix}\right)\right) \tag{38}$$

$$[\boldsymbol{H}_2]_{n,\ell} \approx \exp\left(-j\frac{2\pi}{\lambda}\left(\boldsymbol{e}_{z_2}^\top\begin{bmatrix}x_n''\\y_n''\\z_n''\end{bmatrix} - \boldsymbol{e}_{z_2}^\top\begin{bmatrix}x_\ell'\\y_\ell'\\z_\ell'\end{bmatrix}\right)\right). \tag{39}$$

As all the above channels are of rank-one, the capacities for direct and IRS-assisted transmission are, respectively,

$$\log_2\left(1+N_\mathrm{t}N_\mathrm{r}\mathsf{SNR}_\mathsf{d}\right) \tag{40}$$

and

$$\log_2\left(1+N_\mathrm{t}N_\mathrm{r}M^2\mathsf{SNR}_\mathsf{a}\right). \tag{41}$$

TABLE II
ARRAY DESCRIPTIONS

	Small			Large		
	IRS	AP	Device	IRS	AP	Device
Footprint [cm × cm]	40×40	4×4	2×2	80×80	8×8	4×4
Spacing [cm]	0.05	0.5	0.5	0.05	1	1
Dimensionality	800×800	8×8	4×4	1600×1600	8×8	4×4
Number of elements	640000	64	16	2560000	64	16

VI. Examples and Discussion

To verify the DOF augmentation and ensure that it is not an artifact of the parabolic wavefront approximation, the exact channel models in (2)–(6) are used henceforth, without reliance on that approximation. The considered geometry is illustrated in Fig. 3 while the various parameters are listed in Table I and the array geometries are detailed in Table II. For the sake of generality, the device is randomly oriented and differences in antenna directivity are disregarded (they would merely alter the SNR). The AP is parallel to the xz-plane and, because the channel is considered static and therefore known by both the device and the AP, their roles as transmitter or receiver are interchangeable [26].

Fig. 4 depicts the empirical probability mass function (PMF) of the number of supported signal streams, i.e., the number of spatial subchannels that are allocated positive power in (17) and (27). This is a finite-SNR measure of the DOF. In turn, Fig. 5 depicts the empirical cumulative density function (CDF) of (*i*) the capacity of the direct channel in (17), and (*ii*) the achievable spectral efficiency of the IRS-assisted transmission in (27), with the phase shifts in (28). The distributions are over the device orientation, with 100 random values generated for each figure.

In terms of number of signal streams, the following can be observed:

- The leftmost example corresponds to a small IRS, small AP, and small device; the exact dimensions and antenna numbers are provided in Table II. While the direct channel is essentially rank-one, with the IRS—despite its modest aperture—it becomes possible to spatially multiplex up to five streams.
- In the central example, the IRS is still small while the AP and device are large, such that spatially multiplexing two or three streams is possible over the direct channel. The IRS amplifies that considerably, all the way up to eight streams.
- For the rightmost example, the IRS is large whereas the device and AP are small. Here the impact of the IRS is most dramatic, with the number of signal streams being unity without it and as high as ten with it.

Additional signal streams translate to a stronger spectral efficiency, as confirmed by Fig. 5. While the increase is not proportional to the number of streams, because the per-stream SNR diminishes the improvement is hefty. With the large IRS in particular, the median spectral efficiency is almost six times higher.

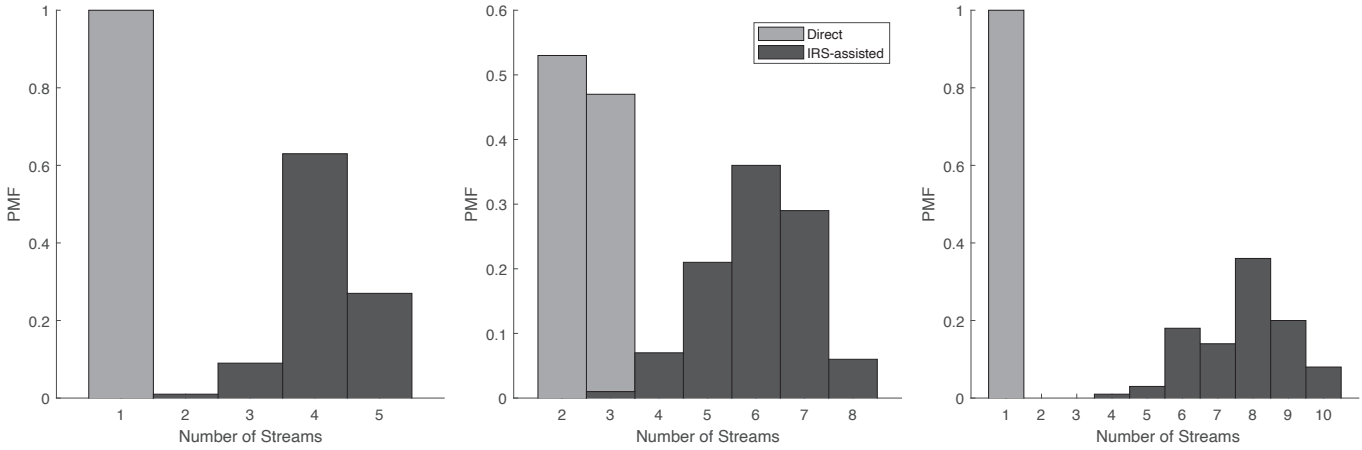

(a) Small IRS, small AP, small device. (b) Small IRS, large AP, large device. (c) Large IRS, small AP, small device.

Fig. 4. PMF of the number of supported signal streams.

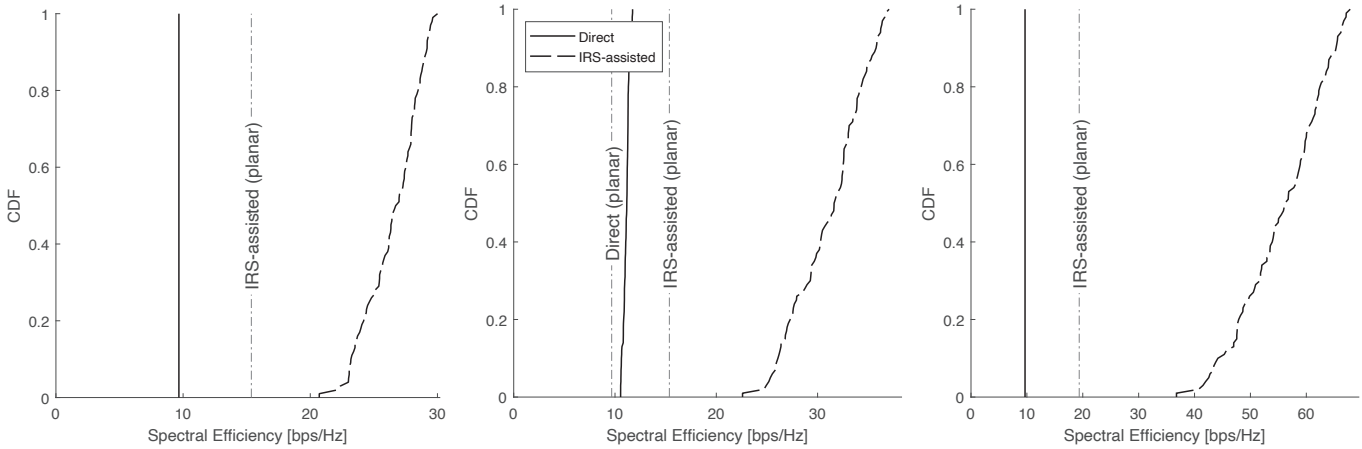

(a) Small IRS, small AP, small device. (b) Small IRS, large AP, large device. (c) Large IRS, small AP, small device.

Fig. 5. CDF of the achievable spectral efficiencies with the exact spherical wavefronts. Also shown, in a thinner stroke, are the capacities, in (40) and (41), under a planar wavefront model.

The benefits of additional DOF are bound to abate as the SNR shrinks, yet an IRS might also be helpful in that regime, to assist in the beamforming, and indeed the bulk of research on IRSs thus far had been on that front [27].

Finally, it is worth comparing the performance observed under the actual spherical wavefronts against what would transpire with a planar wavefront model. The contrast, also illustrated in Fig. 5, is stark. A planar wavefront model is inadequate to characterize the effect that an IRS, even a small one, has on the spectral efficiency when spatial multiplexing is employed. Indeed, a planar model is unable to represent how additional DOF are unlocked by virtue of the IRS being present and hence it grossly underestimates the performance.

VII. Conclusion

Besides increasing the received power and skirting obstructions, IRSs may unlock DOF. Crucially, this DOF augmentation requires no increase in the footprints of transmitter and receiver, nor multipath propagation, but it results from growing the aperture of the IRS itself. This potential is concealed by planar wavefront models, and is only revealed once the curved nature of the wavefronts is accounted for.

It would be of interest to delineate the SNRs beyond which DOF maximization is the appropriate strategy, and seek to blend it with the beamforming approaches that are sure to be preferable at lower SNRs and/or at lower frequencies (where LOS spatial multiplexing is unfeasible). Likewise, the deployment criteria should be harmonized, depending on the application. Increasing the robustness to the wideband effect that arises as the bandwidth grows very broad is another important research avenue [28]–[31].

Acknowledgment

H. Do and N. Lee are supported by the National Research Foundation of Korea (NRF) grant (No.2020R1C1C1013381) and by Institute of Information communications Technology Planning & Evaluation (IITP) grant (No.2021-0-00260, Research on LEO Inter-Satellite Links), both funded by the

Korea government (MSIT). Prof. Lozano is supported by the European Research Council under the H2020 Framework Programme/ERC grant agreement 694974, by the ICREA Academia program, and by the Fractus-UPF Chair on Tech Transfer and 6G.

REFERENCES

[1] H.-J. Song and T. Nagatsuma, "Present and future of terahertz communications," *IEEE Trans. Terahertz Sci. Technol.*, vol. 1, no. 1, pp. 256–263, 2011.

[2] T. S. Rappaport, Y. Xing, O. Kanhere, S. Ju, A. Madanayake, S. Mandal, A. Alkhateeb, and G. C. Trichopoulos, "Wireless communications and applications above 100 GHz: Opportunities and challenges for 6G and beyond," *IEEE Access*, vol. 7, pp. 78 729–78 757, 2019.

[3] V. Petrov, T. Kurner, and I. Hosako, "IEEE 802.15. 3d: First standardization efforts for sub-terahertz band communications toward 6G," *IEEE Commun. Mag.*, vol. 58, no. 11, pp. 28–33, 2020.

[4] J. G. Andrews, S. Buzzi, W. Choi, S. V. Hanly, A. Lozano, A. C. Soong, and J. C. Zhang, "What will 5G be?" *IEEE J. Sel. Areas Commun.*, vol. 32, no. 6, pp. 1065–1082, 2014.

[5] F. Boccardi, R. W. Heath, A. Lozano, T. L. Marzetta, and P. Popovski, "Five disruptive technology directions for 5G," *IEEE Commun. Mag.*, vol. 52, no. 2, pp. 74–80, 2014.

[6] C. Liaskos, S. Nie, A. Tsioliaridou, A. Pitsillides, S. Ioannidis, and I. Akyildiz, "A new wireless communication paradigm through software-controlled metasurfaces," *IEEE Commun. Mag.*, vol. 56, no. 9, pp. 162–169, 2018.

[7] Q. Wu and R. Zhang, "Towards smart and reconfigurable environment: Intelligent reflecting surface aided wireless network," *IEEE Commun. Mag.*, vol. 58, no. 1, pp. 106–112, 2019.

[8] E. Basar, M. Di Renzo, J. De Rosny, M. Debbah, M.-S. Alouini, and R. Zhang, "Wireless communications through reconfigurable intelligent surfaces," *IEEE Access*, vol. 7, pp. 116 753–116 773, 2019.

[9] R. W. Heath, Jr. and A. Lozano, *Foundations of MIMO Communication*. Cambridge University Press, 2018.

[10] P. F. Driessen and G. Foschini, "On the capacity formula for multiple input-multiple output wireless channels: A geometric interpretation," *IEEE Trans. Commun.*, vol. 47, no. 2, pp. 173–176, Feb. 1999.

[11] D. Gesbert, H. Bolcskei, D. A. Gore, and A. J. Paulraj, "Outdoor MIMO wireless channels: Models and performance prediction," *IEEE Trans. Commun.*, vol. 50, no. 12, pp. 1926–1934, 2002.

[12] F. Bøhagen, P. Orten, and G. Øien, "Construction and capacity analysis of high-rank line-of-sight MIMO channels," in *Proc. IEEE Wireless Commun. Netw. Conf.*, Mar. 2005, pp. 432–437.

[13] P. Larsson, "Lattice array receiver and sender for spatially orthonormal MIMO communication," in *Proc. IEEE Veh. Technol. Conf.*, May 2005, pp. 192–196.

[14] I. Sarris and A. R. Nix, "Design and performance assessment of high-capacity MIMO architectures in the presence of a line-of-sight component," *IEEE Trans. Veh. Technol.*, vol. 56, no. 4, pp. 2194–2202, Jul. 2007.

[15] E. Torkildson, U. Madhow, and M. Rodwell, "Indoor millimeter wave MIMO: Feasibility and performance," *IEEE Trans. Wireless Commun.*, vol. 10, no. 12, pp. 4150–4160, 2011.

[16] J.-S. Jiang and M. A. Ingram, "Spherical-wave model for short-range MIMO," *IEEE Trans. Commun.*, vol. 53, no. 9, pp. 1534–1541, 2005.

[17] F. Bøhagen, P. Orten, and G. Øien, "On spherical vs. plane wave modeling of line-of-sight MIMO channels," *IEEE Tran. Commun.*, vol. 57, no. 3, pp. 841–849, 2009.

[18] H. Do, N. Lee, and A. Lozano, "Reconfigurable ULAs for line-of-sight MIMO transmission," *IEEE Trans. Wireless Commun.*, vol. 20, no. 5, pp. 2933–2947, 2020.

[19] ——, "Capacity of line-of-sight MIMO channels," in *Int'l Symp. Inform. Theory (ISIT'20)*, 2020, pp. 2044–2048.

[20] H. Do, S. Cho, J. Park, H.-J. Song, N. Lee, and A. Lozano, "Terahertz line-of-sight MIMO communication: Theory and practical challenges," *IEEE Commun. Mag.*, vol. 59, no. 3, pp. 104–109, 2021.

[21] H. Do, N. Lee, and A. Lozano, "Rotatable URAs for line-of-sight MIMO transmission," in *IEEE Global Commun. Conf. (GLOBECOM)*, 2021.

[22] D. A. Miller, "Communicating with waves between volumes: evaluating orthogonal spatial channels and limits on coupling strengths," *Applied Optics*, vol. 39, no. 11, pp. 1681–1699, 2000.

[23] H. Do, N. Lee, and A. Lozano, "Line-of-sight MIMO via intelligent reflecting surface," *IEEE Trans. Wireless Commun.*, vol. 22, 2023.

[24] M. Dunna, C. Zhang, D. Sievenpiper, and D. Bharadia, "ScatterMIMO: Enabling virtual MIMO with smart surfaces," in *Proc. Annu. Int. Conf. Mobile Comput. Netw.*, 2020, pp. 1–14.

[25] Q. Wu, S. Zhang, B. Zheng, C. You, and R. Zhang, "Intelligent reflecting surface-aided wireless communications: A tutorial," *IEEE Trans. Commun.*, vol. 69, no. 5, pp. 3313–3351, 2021.

[26] A. Tulino, A. Lozano, and S. Verdú, "MIMO capacity with channel state information at the transmitter," in *IEEE Int'l Symp. Spread Spectrum Techn. and Applic. (ISSSTA'04)*, 2004.

[27] S. Gong, X. Lu, D. T. Hoang, D. Niyato, L. Shu, D. I. Kim, and Y.-C. Liang, "Toward smart wireless communications via intelligent reflecting surfaces: A contemporary survey," *IEEE Commun. Surv. & Tut.*, vol. 22, no. 4, pp. 2283–2314, 2020.

[28] B. Wang, F. Gao, S. Jin, H. Lin, G. Li, S. Sun, and T. Rappaport, "Spatial-wideband effect in massive MIMO with application in mmWave systems," *IEEE Commun. Mag.*, vol. 56, no. 12, pp. 134–141, 2018.

[29] M. M. Mojahedian, M. Attarifar, and A. Lozano, "Spatial-wideband effect in line-of-sight MIMO communication," in *IEEE Int. Conf. Commun. (ICC)*, June 2022.

[30] M. Attarifar, M. M. Mojahedian, and A. Lozano, "Reduced-complexity wideband line-of-sight MIMO communication," in *Asilomar Conf. on Signals, Systems and Computers*, 2022.

[31] M. M. Mojahedian, M. Attarifar, and A. Lozano, "DFT-Based wideband line-of-sight MIMO communication," in *IEEE Global Commun. Conf. (GLOBECOM)*, Dec. 2022.